A coronagraphic absorbing cloud reveals the narrow-line region and extended Lyman α emission of QSO J0823+0529[★]

H. Fathivavsari,[1]† P. Petitjean,[1]† P. Noterdaeme,[1]† I. Pâris,[2] H. Finley,[3,4] S. López,[5] R. Srianand[6] and P. Sánchez[5]

[1]*Institut d'Astrophysique de Paris, Université Paris 6-CNRS, UMR7095, 98bis Boulevard Arago, F-75014 Paris, France*
[2]*Osservatorio Astronomico di Trieste, via G. B. Tiepolo 11, I-34131 Trieste, Italy*
[3]*CNRS/IRAP, 14 Avenue E. Belin, F-31400 Toulouse, France*
[4]*University Paul Sabatier of Toulouse/ UPS-OMP/ IRAP, F-31400 Toulouse, France*
[5]*Departamento de Astronomía, Universidad de Chile, Casilla 36-D, Santiago, Chile*
[6]*Inter-University Centre for Astronomy and Astrophysics, Post Bag 4, Ganeshkhind, 411 007 Pune, India*

ABSTRACT

We report long-slit spectroscopic observations of the quasar SDSS J082303.22+052907.6 ($z_{\rm C IV} \sim 3.1875$), whose broad-line region (BLR) is partly eclipsed by a strong damped Lyman α (DLA; $\log N({\rm H I}) = 21.7$) cloud. This allows us to study the narrow-line region (NLR) of the quasar and the Lyman α emission from the host galaxy. Using CLOUDY models that explain the presence of strong N V and P V absorption together with the detection of Si II* and O I** absorption in the DLA, we show that the density and the distance of the cloud to the quasar are in the ranges $180 < n_{\rm H} < 710$ cm^{-3} and $580 > r_0 > 230$ pc, respectively. Sizes of the neutral ($\sim$2–9pc) and highly ionized phases ($\sim$3–80pc) are consistent with the partial coverage of the C IV BLR by the C IV absorption from the DLA (covering factor of $\sim$0.85). We show that the residuals are consistent with emission from the NLR with C IV/Lyman α ratios varying from 0 to 0.29 through the profile. Remarkably, we detect extended Lyman α emission up to 25 kpc to the north and west directions and 15 kpc to the south and east. We interpret the emission as the superposition of strong emission in the plane of the galaxy up to 10 kpc with emission in a wind of projected velocity $\sim$500 km s^{-1} which is seen up to 25 kpc. The low metallicity of the DLA (0.27 solar) argues for at least part of this gas being infalling towards the active galactic nucleus and possibly being located where accretion from cold streams ends up.

Key words: galaxies: evolution – intergalactic medium – quasars: absorption lines – quasars: individual: SDSS J082303.22+052907.6.

1 INTRODUCTION

Luminous high-redshift quasars consist of supermassive black holes residing at the centre of massive galaxies and growing through mass accretion of gas in an accretion disc. Bright quasars play an important role in shaping their host galaxies through the emission of ionizing flux but also through launching powerful and high-velocity outflows of gas. These outflows inject energy and material to the disc of the galaxy and may be influencing the physical state up to larger distances. It has remained unclear however what are the

mechanisms that drive energy from the very centre of the active galactic nuclei (AGNs) to the outskirts of the galaxy.

Observational evidence for outflows and winds in AGNs is seen as prominent radio jets in radio-loud sources, broad absorption lines (BALs) observed in BAL quasars, or through the photoionized warm absorber (WA) which is frequently observed in the soft X-rays (e.g. Crenshaw, Kraemer & George 2003). Gravitational micro-lensing studies have shown that the primary X-ray emission region in AGN is of the order of a few tens of gravitational radii in size (e.g. Dai et al. 2010) and X-ray spectroscopy shows that highly ionized outflows launched from this region are seen in high-z quasars (Chartas et al. 2009) and in at least 40 per cent of them with velocities up to 0.1 c (Gofford et al. 2013).

Outflows are observed also on large scales. Mullaney et al. (2013) used the Sloan Digital Sky Survey (SDSS) spectroscopic data base to study the one-dimensional (1D) kinematic properties

of [O III] λ5007 by performing multicomponent fitting to the optical emission-line profiles of about 24 000, $z < 0.4$ optically selected AGNs. They showed that approximately 17 per cent of the AGNs have emission-line profiles that indicate their ionized gas kinematics are dominated by outflows and a considerably larger fraction are likely to host ionized outflows at lower levels. Harrison et al. (2014) find high-velocity ionized gas (velocity widths of about 600–1500 km s^{-1}) with observed spatial extents of (6–16) kpc in a representative sample of $z < 0.2$, luminous (i.e. L[O III] $>$ $10^{41.7}$ erg s^{-1}) type 2 AGNs. Therefore, galaxy-wide energetic outflows are not confined to the most extreme star-forming galaxies or radio-luminous AGNs.

If outflows are observed both on small and large scales, how the small-scale outflows are transported at larger distances remains unclear (Faucher-Giguere & Quataert 2012; Ishibashi & Fabian 2015; King & Pounds 2015). This is however a crucial question as these outflows are massive and energetic enough to significantly influence star formation in the host galaxy and provide significant metal enrichment to the interstellar medium (ISM) and intergalactic medium (e.g. Dubois et al. 2013). At high redshift where quasars are more luminous, the consequences of such outflows are of first importance for galaxy formation. One way to study the interplay between the quasar and its surrounding is to search for Lyman α emission around quasars (e.g. Hu & Cowie 1987; Hu, McMahon & Egami 1996; Petitjean et al. 1996; Bunker et al. 2003; Christensen et al. 2006). These observations reveal gas infalling on to the galaxy (Weidinger et al. 2005), positive feedback from the AGN (Rauch et al. 2013) or a correlation between the luminosity of the extended emission and the ionizing flux from the quasar (North et al. 2012).

Very recently, we searched quasar spectra from the SDSS-III Baryon Oscillation Spectroscopic Survey (BOSS; Dawson et al. 2013) for the rare occurrences where a strong damped Lyman α (DLA) absorber blocks the broad-line region (BLR) emission from the quasar and acts as a natural coronagraph to reveal narrow Lyman α emission from the host galaxy (Finley et al. 2013; see also Hennawi et al. 2009). This constitutes a new way to have direct access to the quasar host galaxy and possibly, when the size of the DLA is small enough, to the very centre of the AGN. Out of a total of more than 70 000 spectra of $z > 2$ quasars (Pâris et al. 2012), we gathered a sample of 57 such quasars and followed-up six of them with the slit spectrograph Magellan-MagE to search for the very special cases where the DLA coronagraph reveals the very centre of the host galaxy and extended Lyman α emission. In the course of this follow-up programme, we found one object SDSS J0823+0529 where the DLA does not cover the Lyman α BLR entirely and reveals the emission of the Lyman α and C IV narrow-line regions (NLRs). We show here that this is a unique opportunity to study the link between the properties of the central regions of the AGN to that of the gas in the halo of the quasar.

The paper is organized as follows. In Section 2, we describe the observations and data reduction. We derive properties of the gas associated with the DLA (metallicity, ionization state, density, distance to the quasar, typical size) in Section 3. We discuss the properties of the quasar NLR and of the extended Lyman α emission in Sections 4 and 5, respectively, We then finally present our conclusions in Section 6. In this work, we use a standard cold dark matter cosmology with $\Omega_\Lambda = 0.73$, $\Omega_m = 0.27$, and $H_0 = 70$ km s^{-1} Mpc^{-1} (Komatsu et al. 2011). Therefore, 1 arcsec corresponds to about 7.1 kpc at the redshift of the quasar ($z = 3.1875$ see below). In the following, we will use solar metallicities from Asplund et al. (2009).

2 OBSERVATIONS AND DATA REDUCTION

The spectrum of the quasar SDSS J0823+0529 was observed with the Magellan Echellette spectrograph (MagE; Marshall et al. 2008) mounted on the 6.5 m Clay telescope located at Las Campanas Observatory. MagE is a medium-resolution long-slit spectrograph that covers the full wavelength range of the visible spectrum (3200 Å to 1 μm). Its 10 arcsec long slit and 0.30 arcsec per pixel sampling in the spatial direction, are ideal for observing high-redshift extended astrophysical objects. The spectrograph was designed to have high throughput in the blue, with the peak throughput reaching 22 per cent at 5600 Å including the telescope.

The quasar was observed in 2012 December with an 1 arcsec width slit aligned along two different position angles (PAs) for 1 h each. One position was south–north (PA = 0) and the other position was east–west (PA = 90). Another 1 h exposure with PA = 90 was taken in 2013 February but the resultant spectrum has a lower signal-to-noise ratio (SNR). Following each exposure, the spectrum of a standard star was also recorded allowing us to precisely flux calibrate the quasar spectra. The seeing, measured on the extracted trace of the quasar is 1.06 arcsec for PA = 0 and 0.93 arcsec for PA = 90.

We reduced the spectrum using the Mage_Reduce pipeline written in the Interactive Data Language (IDL) by George Becker.[1] In addition to the 1D spectrum, the pipeline provides two-dimensional (2D) sky-subtracted science frames as well as the corresponding 2D wavelength solution corrected for the vacuum heliocentric velocity shifts. These 2D images will later be used to rectify the curved spectral orders (see below). Here, we note that since there is an extended Lyman α emission in order 9 of our 2D spectra, we preferentially used a wider extraction window to extract this order.

2D spectra when imaged on to a detector are often curved with respect to the natural (x, y)-coordinate system of the detector defined by the CCD columns (Kelson 2003). To rectify the curvature of the orders, we first rebin the wavelength area (given by the 2D wavelength solution) and position area (given by the 2D slitgrid array provided by the pipeline) increasing the number of pixel by a factor of 100. We define a new 2D array, with one dimension representing the wavelength (λ) and the other the position on the slit (s). For each pixel on the 2D spectrum of the quasar, we take its corresponding wavelength and its position on the slit directly in the rebinned 2D areas. Therefore, the (x, y) coordinates of each pixel (defined by the CCD columns) can now be transformed to an (s, λ) coordinate defined by the new 2D array introduced above. In this new (s, λ)-coordinate system, the curvature of the orders and the tilting of the spectral lines are all rectified. In this study, we use these rectified 2D images when we discuss the spatial extension of the Lyman α emission line in the quasar spectrum. Note that the rebinning process has very little effect on the Lyman α emission because it is conveniently placed in the middle of the corresponding order where curvature is at minimum.

Finally, the extracted 1D spectrum of each individual order is corrected for the relative spectral response of the instrument and flux calibrated using the spectrum of a standard star (HR 1544) observed during the same night. The spectrum of the standard star can be found in the European Southern Observatory standard star catalogue webpage.[2] We emphasize that our standard star spectrum was obtained immediately after observing the quasar spectrum. We

---

[1] ftp://ftp.ast.cam.ac.uk/pub/gdb/mage_reduce/
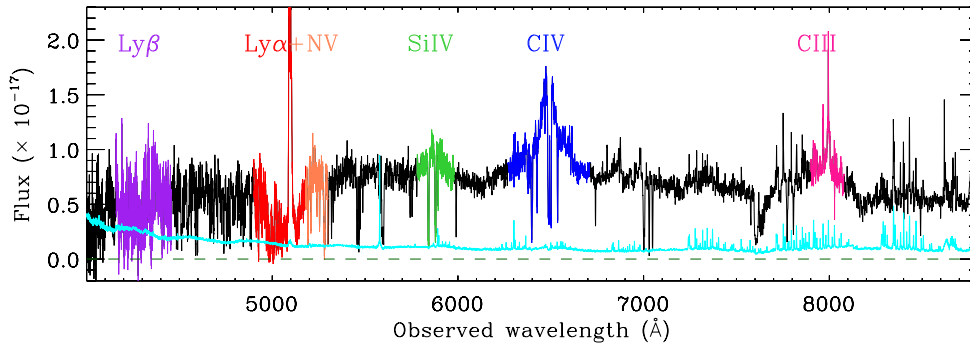[2] https://www.eso.org/sci/observing/tools/standards.html

Figure 1. Flux-calibrated spectrum of the quasar SDSS J0823+0529 over the full observed wavelength range. The positions of broad emission lines are shown with different colours. The Lyman α-N v broad emission is absorbed by a strong DLA and a strong narrow Lyman α emission is revealed. The cyan curve shows the corresponding error array. The *y*-axis is in erg s^{-1} cm^{-2} Å^{-1}.

also flux calibrated in the same way the 2D spectra in the Lyman α range. These flux-calibrated spectra are then combined weighting each pixel by the inverse of its variance. The resulting spectrum (after binning with a 3 × 3 box) has $\sim$27 km s^{-1} per pixel and 3 pixels per resolution element, and therefore FWHM $\sim$80 km s^{-1}.

We have fitted the quasar C IV emission line with two Gaussian functions (to mimic the two lines of the doublet) to estimate the redshift of the quasar. We derive $z_{em} = 3.1875$. This is $\sim$330 km s^{-1} smaller than the redshift of the DLA ($z_{DLA} = 3.1910$ derived from the fit of Si II and Fe II absorptions). However, it is well known that redshifts from C IV are smaller by up to 600 km s^{-1} compared to redshifts from narrow forbidden lines (e.g. Hewett & Wild 2010). Therefore, we cannot be certain that the DLA is redshifted compared to the quasar. We would need to detect [O III] lines redshifted to the infrared to have a better estimate of z_{em}.

3 A DLA ACTING AS A CORONAGRAPH

Fig. 1 shows the co-added spectrum of SDSS J0823+0529 using all the exposures taken at different PAs. It is apparent that a strong DLA is located close to the redshift of the quasar. However, strong Lyman α emission is present in the centre of the DLA trough. This is possible if the absorbing cloud has a transverse extension which is smaller than the central NLR of the quasar. Note that the strength of the Lyman α emission together with the size of the cloud derived below makes it very improbable that the Lyman α emission could be a consequence of star formation in the DLA itself.

The redshift of the DLA ($z_{DLA} = 3.1910$) was determined by conducting a simultaneous Voigt profile fit of the Fe II, Si II*, and O I** absorption profiles.

3.1 Elemental abundances

A Voigt profile fit was conducted on the DLA absorption line of this system, resulting in a neutral hydrogen column density of log $N_{HI} = 21.70 \pm 0.10$. Note that the placement of the quasar continuum is very uncertain as the DLA covers the Lyman α and the N v broad emission lines. However, the core and especially the red wing of the DLA profile allowed us to satisfactorily constrain the H I column density. We will come back to this in Section 3.4.

We detect absorption lines from O I, O I**, Si II, Si II*, Fe II, Al II, Al III, Ar I, C II, C II*, C IV, Si IV, P V, and N V. Absorption profiles are shown in Fig. 2 and results from fitting these lines are given in Tables 1 and 2. Techniques used here are similar to those in Fathivavsari et al. (2013). It must be noted that most of the lines are

saturated, preventing us from deriving accurate column densities especially at the resolution of our data ($R \sim 4000$).

The profiles are dominated by a main strong component clearly seen in particular in Fe II λ1608 and Si II* λ1533. To constrain the Doppler parameter of this component, we take advantage of the fact that Fe II λ1608 is not saturated and well defined while Fe II λ1611 is not detected (see Fig. 3). We start by fitting together Si II λ1808 and 1526, imposing the presence of the main component with a fixed Doppler parameter. We then use the resulting decomposition to fit the Fe II lines. Results are shown in Fig. 3 for $b = 10$ and 20 km s^{-1}. It is apparent that components narrower than $b \sim 20$ km s^{-1} are not favoured and $b = 10$ km s^{-1} is definitely rejected. Therefore, we are confident that imposing $b \sim 20$ km s^{-1} for the main component in the DLA will give us a good estimate of column densities.

For some of the species, several lines with very different oscillator strengths (either in doublets or multiplets) are present so that we can derive robust estimates of the column densities. This is the case for Si II, Si II*, and Fe II. From this, we derive metallicities relative to solar, [Si/H] $= -0.79$ and [Fe/H] $= -1.87$. We also derive an upper limit on N(Fe III).

We also fit the high-ionization species. We did not try to tie the components in different profiles because this high-ionization phase could be highly perturbed. In Table 2, except for the first two components of the C IV absorption profiles, all reported column densities are upper limits because the profiles are strongly saturated. It can be seen however that the decompositions in sub-components are fairly consistent between the different species.

We detect absorptions from O I** and Si II* which are rarely detected in DLAs (see Noterdaeme et al. 2015; Neeleman, Prochaska & Wolfe 2015) and are more commonly seen in DLAs associated to Gamma Ray Burst (GRB) afterglows (Vreeswijk et al. 2004; Chen et al. 2005; Fynbo et al. 2006). Absorption from the fine structure state of Si II will be used to constrain the density of the absorbing cloud (see below).

The high measured depletion of iron relative to silicon (i.e. [Si/Fe] $= +1.08$) in this DLA suggests the presence of dust. Consequently, extinction due to dust might be significant along this line of sight. Indeed, the median $g - r$ colour for a sample of 697 non-BAL quasars with redshift within $\Delta z = \pm 0.02$ around $z_{em} = 3.1910$ is $\langle g - r \rangle = 0.30$ when $g - r = 1.1$ for QSO J0823+0529. The reddening for this line of sight is $E(B - V) = 0.09$, measured with an Small Magellanic Cloud (SMC) reddening law template, which places it among the most reddened of the sightlines in the Finley et al. (2013) statistical sample. We will take this reddening into account in the following while discussing the properties of the quasar.
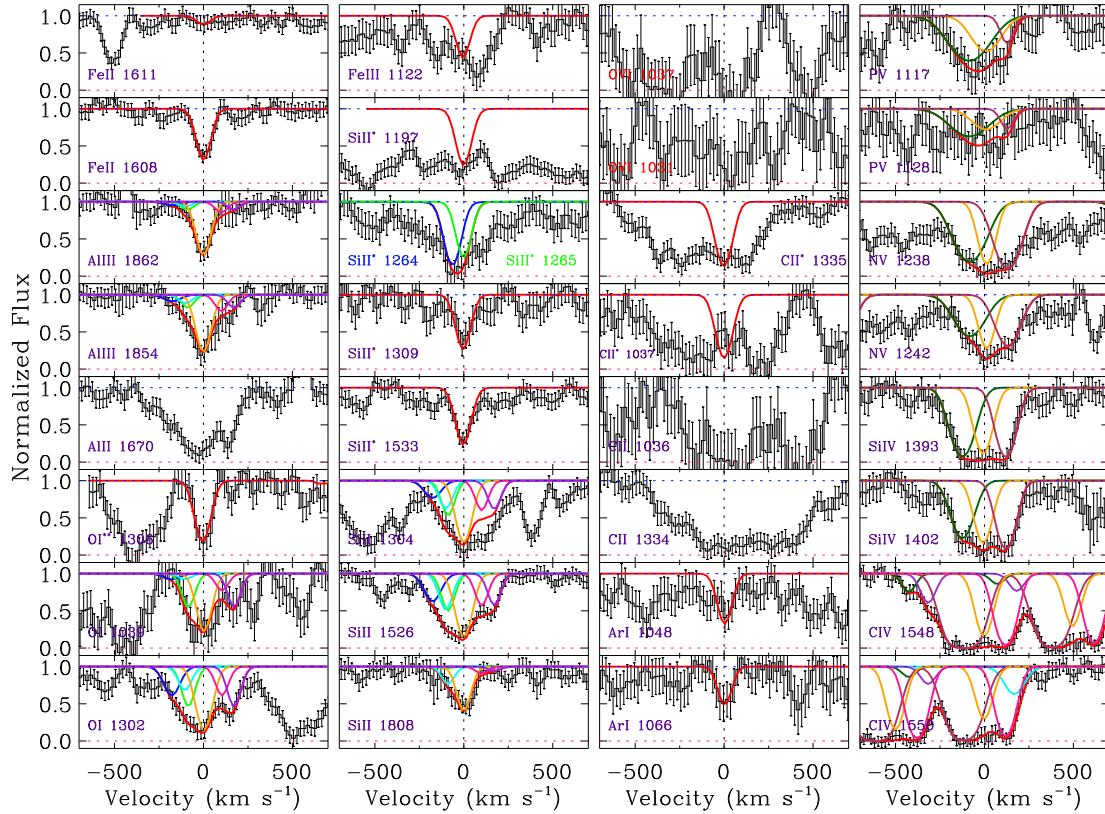
Figure 2. Absorption profiles detected in the DLA at $z_{abs} = 3.1910$. This redshift is used as the origin of the velocity scale. Multicomponent Voigt profile fits were performed on the absorption profiles and the results are shown by red lines together with individual components plotted in different colours. Single component fits were performed on the O I**, Si II*, and Ar I absorption lines. Regions corresponding to the Al II, C II, and O VI are not fitted due to the contaminations by some unidentified absorption lines.
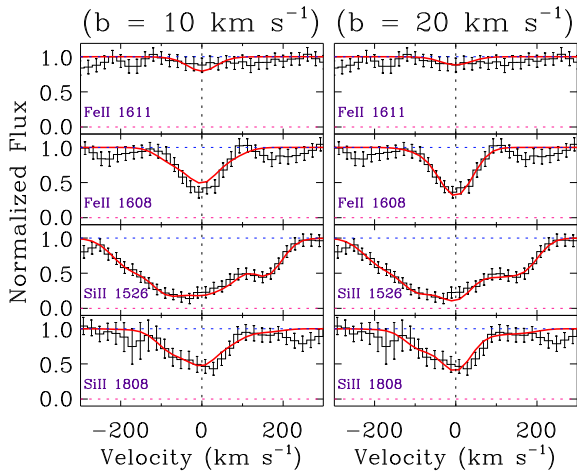

Figure 3. The relative optical depths of Fe II λ1608 and 1611 are used to constrain the Doppler parameter of the main DLA component. The fit is constrained by Si II profiles. In each column, the Doppler parameter of the strong central component is fixed to the value indicated at the top.

3.2 Physical conditions in the DLA gas

In this section, we use the photoionization code CLOUDY to constrain the ionization state of the absorber and its distance to the quasar central engine. Observed ionic ratios of Si II, Si IV, Al III, and Ar I are used to constrain the plane-parallel models constructed for a range of ionization parameters. The calculations were stopped when a

Table 1. Column densities of low-ionization species. The quoted redshift is the redshift of the strongest component in the low ion species.

Redshift	Ion	$\log(N)^a$ observed	$\log(N)$ model
3.190974	Si II	16.42 ± 0.10	16.53
	Si II*	15.49 ± 0.30	15.49
	Fe II	15.33 ± 0.20	16.50
	Fe III	≤ 15.00	15.09
	Ar I	14.97 ± 0.20	15.04
	Al III	14.80 ± 0.10	14.64
	O I**	16.45 ± 0.45	15.70
	O I	17.08 ± 0.50	17.62

Note. ^{a}The Doppler parameter is fixed at $20\,\mathrm{km\,s^{-1}}$ (see Fig. 3).

neutral hydrogen column density of $\log N(\mathrm{H\,I}) = 21.70$ is reached. Solar relative abundances are assumed and the metallicity is taken to be $Z = 0.16\,Z_\odot$ from the silicon abundance of the DLA derived in Section 3.1.

The ionizing spectrum incident on the cloud is taken as the combination of the standard AGN spectrum of Mathews & Ferland (1987), Haardt–Madau extragalactic spectrum (Haardt & Madau 1996) and the Cosmic Microwave Background (CMB) radiation both at $z = 3.1910$. Fig. 4 summarizes the results of these calculations. Bottom panel gives resulting ionic ratios and top panel shows column densities. In both panels, measurements and upper limits are indicated by dashed lines. For Al II, we scale the Si II column density assuming solar metallicity ratios.

Table 2. Column densities of high-ionization species.

Redshift	Ion	b (km s^{-1})	log(N) observed	log(N) model[a]
3.185037	C IV	23	13.60 ± 0.10	
3.186553	C IV	32	13.90 ± 0.10	
3.189333	C IV	86 ± 10	≥15.40 ± 0.10	
3.190953	C IV	38 ± 14	≥14.65 ± 0.30	
3.192634	C IV	39 ± 6	≥15.40 ± 0.50	
Total(C IV)			≥15.75	18.43
3.189333	Si IV	56 ± 10	≥14.30 ± 0.10	
3.190953	Si IV	25 ± 14	≥14.60 ± 0.60	
3.192634	Si IV	25 ± 6	≥15.72 ± 0.90	
Total(Si IV)			≥15.75	16.14
3.189821	N V	99 ± 39	≥14.80 ± 0.30	
3.191157	N V	34 ± 29	≥14.89 ± 0.20	
3.192807	N V	74 ± 19	≥14.87 ± 0.10	
Total(N V)			≥15.33	16.55
3.189788	P V	136	≥14.20 ± 0.20	
3.191109	P V	97	≥13.95 ± 0.30	
3.192757	P V	13	≥13.80 ± 0.60	
Total(P V)			≥14.50	15.30

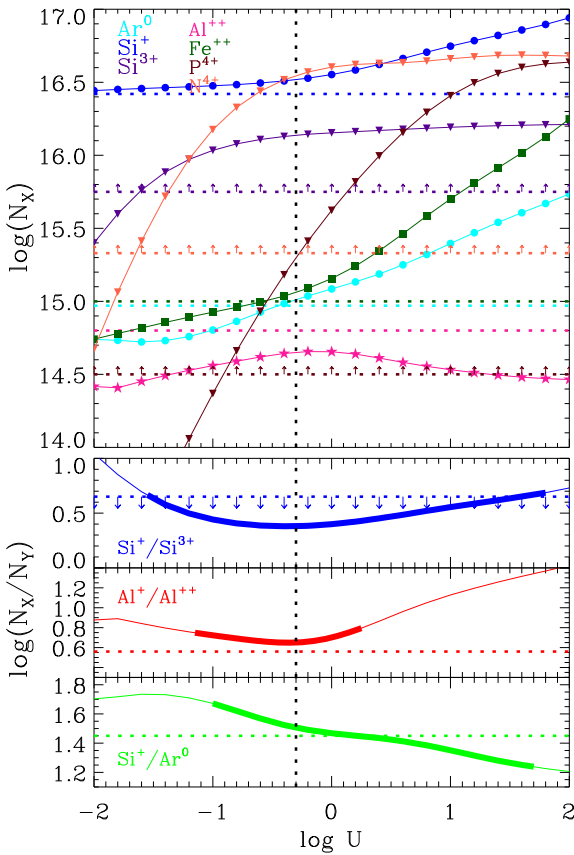*Note.* [a]The Model values are for the ionization parameter log $U = -0.3$.

Figure 4. Results of CLOUDY models of the DLA system. Bottom panel gives resulting ionic ratios and top panel shows column densities. In both panels, measurements are shown by dashed horizontal lines and upper limits are indicated with arrows. The thick lines in the bottom panel show the range of ionization parameters constrained by each ionic ratio.

Table 3. Hydrogen density (n_H) in the cloud, its distance to the central AGN (r_0), size of the DLA (l_{HI}), and transverse size of the C IV phase for different values of the ionization parameter (U).

log U	n_H (cm^{-3})	r_0 (pc)	l(H I) (pc)	l(C IV) (pc)
−1.1	710	579	2.3	3.0
−0.7	500	435	3.2	5.8
−0.3	355	326	4.6	14.6
+0.0	250	275	6.5	33.7
+0.3	180	229	9.1	80.0

The column density ratio log N(Al II)/N(Al III) yields ionization parameter ranging from −1.1 to 0.3. Both log N(Si II)/N(Ar I) ratio and the limit on log N(Si II)/N(Si IV) are consistent with this range of ionization parameters. Our preferred value is log $U = -0.3$ and we indicate the column densities for this model in Tables 1 and 2. Note that we detect a trough at the position of P V λ1117 with an absorption profile which is consistent with that of other high-ionization species (see Fig. 2). The second weaker line of the doublet, P V λ1128 is affected by noise. The fit to these two lines gives a column density which is consistent with the results of the preferred model. The same is true for N V. This strongly supports the fact that the cloud is highly ionized.

To determine the hydrogen density of this cloud (i.e. n_H), a series of CLOUDY models with fixed ionization parameter (varying from log $U = -1.1$ to 0.3) and varying n_H were constructed. Note that in this series of models, the metallicity and incident radiation are the same as those considered above. By increasing the hydrogen density we are indeed trying to collisionally populate the excited states of the Si II ground state to explain the observed Si II* column density.

Knowing the ionization parameter and the density, we can derive the distance of the cloud to the quasar by estimating the number of ionizing photons emitted by the quasar. Since the quasar is reddened, we first estimate the flux at 20370 Å (corresponding to H β at the redshift of the quasar) by extrapolating with a power law the continuum observed at 6125 and 8165 Å. Following Srianand & Petitjean (2000), we then assume that the de-reddened quasar continuum is a power law ($f_\lambda \sim \lambda^{\alpha_\lambda}$; with $\alpha_\lambda = -1.5$) and we consider that the flux at ∼20370 Å is not affected by the reddening. We thus estimate the flux at the Lyman limit in the rest frame of the absorber to be $f_{912\,Å} = 3.40 \times 10^{-17}$ erg s^{-1}cm^{-2}Å^{-1}. This flux corresponds to a luminosity of $L_{912\,Å} = 3.25 \times 10^{42}$ erg s^{-1} Å^{-1} at the Lyman limit. We can now estimate the rate at which hydrogen ionizing photons are impinging upon the face of the cloud by integrating $L_\nu/h\nu$ over the energy range 1–20 Ryd. If we assume a flat spectrum for the quasar over this energy range, we get $Q = 6.78 \times 10^{55}$ photons per second. From the definition of the ionization parameter U,

$$U = \frac{Q}{4\pi r_0^2 n_H c} \tag{1}$$

one can see that for given values of n_H, U, and Q, one can uniquely estimate the distance, r_0, from the quasar to the absorbing cloud (c is the speed of light).

We can then derive the size of the cloud along the line of sight. For the neutral part, the size along the line of sight is $l \sim N_{HI}/n_H$. Results are summarized in Table 3 which gives the hydrogen density, distance to the quasar and size of the neutral phase of the cloud for different values of log U. The longitudinal size range from 2.3 to 9.1 pc for a distance of, respectively, 579–229 pc from the quasar and a hydrogen density of 710–180 cm^{-3}. Using the structure given by the model and assuming that the cloud is spherical we can derive
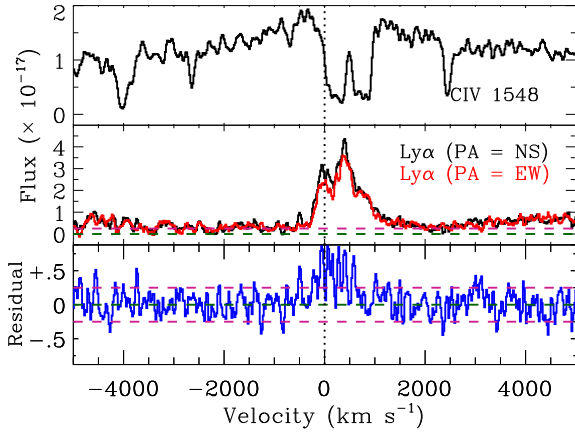
Figure 5. Top panel shows on a velocity scale the quasar C IV emission and C IV absorptions from the DLA. The Lyman α regions for the two PAs (PA = NS in black, PA = EW in red) are overplotted in the middle panel. The DLA trough never reaches the zero level. Bottom panel shows the subtraction of the two spectra (note the change in the *y*-scale). The residual is consistent in the two spectra. Note that the *y*-axis is in erg s^{-1} cm^{-2} Å^{-1}.

the transverse size of the C IV phase. It is given in the last column of Table 3 and range from 3 to 80 pc. These estimates for the transverse size of the high-ionization zone are only rough estimates because our model is very simple (only one density) and we assume spherical geometry.

3.3 Residual flux in the bottom of the DLA trough

We observe residual flux in the bottom of the DLA trough extending in velocity well beyond the narrow emission line. This can be seen in Fig. 5 where we overplot zooms of the Lyman α regions observed along the two PAs. It is apparent that the flux is never at zero in the trough. We checked in the Lyman α forest that the bottom of saturated lines have on an average zero flux. The residual flux is consistent in these two spectra as is demonstrated in the bottom panel of the figure which gives the difference between the two spectra.

This means that the DLA cloud does not cover the background source completely. Since the source of the quasar continuum is much smaller than the BLR (e.g. Hainline et al. 2013), this excess is due either to the cloud not covering the BLR completely or to a second continuum source.

We investigate here if this excess can be due to an additional continuum source. If this excess is due to the continuum of the host galaxy then we would expect some residual at the bottom of metal lines. Indeed C II λ1334 is saturated and seems to show some weak residual (see Fig. 2). We thus have scaled the LBG mean continuum as given by Kornei et al. (2010) to the bottom of C II λ1334. We find that this could explain 20–50 per cent of the DLA residual. The corresponding magnitude of the galaxy would be 23.22 which would be very bright. In any case, this possibility cannot explain all the residual.

It is probable that part of the residual flux in the bottom of the DLA trough is due to the fact that part of the Lyman α emission from the BLR is not covered by the DLA. The size of the BLR can be inferred from time delay measurements between variations in the continuum and in the broad lines. Recent investigations of low-redshift AGNs show a tight relation between this size and the luminosity of the AGN, $R = A \times (L/10^{43})^B$, where *R* is the radius of the BLR, *A* is a typical distance in light-days, and *L* is the luminosity either in an emission line (H β or C IV) or in the continuum. The
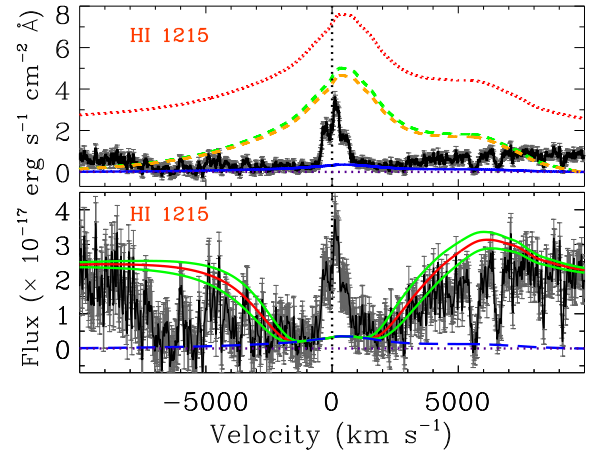

Figure 6. Upper panel: the residual in the bottom of the DLA trough seen over the velocity range [−3000, +3000] km s^{-1} can be explained if ∼10 per cent of the broad-line region is not covered (solid blue line). The de-reddened QSO spectrum (dotted red curve) recovered from PCA analysis of the red part of the spectrum is used to estimate the quasar emission lines (dashed green line) that are then scaled to derive the covering factor of the cloud. Lower panel: the red curve is the DLA fit conducted on the de-reddened observed spectrum. Green curves indicate the ±1σ limits.

index is found to have a value close to *B* ∼ 0.6–0.7 when the typical distance *A* is in the range 20–80 light-days for local AGNs (Wu et al. 2004; Kaspi et al. 2005). More recently, Bentz et al. (2009a, 2009b) find log (R_{BLR}) = *K* + αlog(λL_λ(5100 Å)) with $\alpha = 0.519^{+0.063}_{-0.066}$ and $K = -21.3^{+2.9}_{-2.8}$. The slope suggests that brighter AGNs have to a first approximation the same structure as fainter AGNs with only larger dimensions. Therefore, extending the Kaspi et al. (2005) relation to higher luminosities yields a typical radius of the order of 1 pc for the BLR of bright high-*z* quasars. In the present case, luminosity is $L_{\mathrm{C\,IV}} \sim 9 \times 10^{44}$ erg s^{-1} which gives a size of the BLR of ≤1.1 pc. We have estimated in the previous section that the longitudinal size of the DLA is of the order of 2–9 pc. This is larger than the size of the BLR. It therefore would mean either that the cloud is much smaller in the transverse direction, corresponding possibly to a filamentary structure or that some holes are present in the cloud or that the cloud is not centred on the quasar.

3.4 QSO BLR Lyman α emission and covering factor

To determine the H I column density accurately, one needs to reconstruct the shape of the quasar spectrum at the position of the DLA profile. We can apply principal component (principle component analysis (PCA)) reconstruction of the quasar flux using the red part of the spectrum to estimate the shape of the Lyman α-N V emission (Pâris et al. 2011, 2014). To do so, we first subtract the residual flux seen at the bottom of the DLA (i.e. residuals from Broad Emission Line (BEL) and narrow emission-line (NEL) regions) so that we get zero flux in the DLA trough. We then de-redden this spectrum and add again the residuals subtracted above. We now have the complete de-reddened observed spectrum. Applying the PCA method on this spectrum, we derive the PCA spectrum shown as the dotted red curve in the upper panel of Fig. 6. Then, we subtract the continuum from the PCA spectrum (green dashed curve) and scale it so that it is consistent with the residual flux seen at the bottom of the DLA trough (solid blue curve). This residual flux is only ∼7 per cent of that of the Lyman α broad emission, indicating that ∼93 per cent of the Lyman α BLR is covered by the cloud.
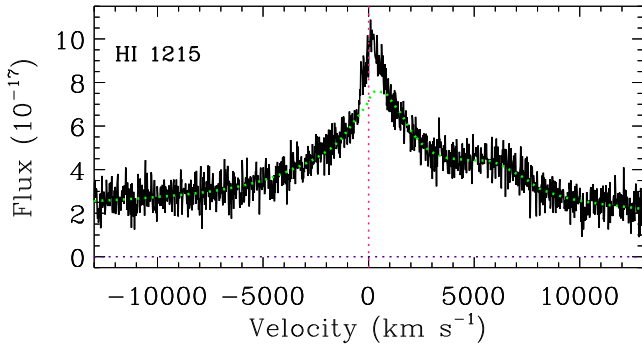
Figure 7. Reconstructed quasar spectrum as it would be observed if no absorption were present. The original PCA spectrum is overplotted as a dotted green curve. The *y*-axis is in erg s^{-1} cm^{-2}Å^{-1}.

To obtain the flux seen by the DLA, we subtract from the dashed green curve the residual flux seen at the bottom of the DLA (i.e. the solid blue curve) and re-add the continuum. We then fit the DLA to obtain the solid red curve in the lower panel. We also checked that we get the same result if, before fitting the DLA, we first re-redden the PCA continuum. As can be seen in Fig. 6, the fit is slightly high near the N v emission line although within errors. This is possibly because the N v emission line in this quasar may be weaker than what is predicted by the PCA method. It should be reminded that the PCA reconstruction is an estimate of the quasar spectrum which stays close to the median spectrum in the overall quasar population (see Pâris et al. 2011). The result (log N(H I) $= 21.7 \pm 0.1$) is consistent with what was derived previously.

Fig. 7 shows the quasar spectrum as it would be observed if no DLA were present. In this figure, we have added the Lyman α narrow emission component seen in the DLA trough to the PCA spectrum. The final spectrum is degraded to the SNR ~20 by adding Gaussian noise to it. It is apparent from this spectrum that the emission from the NLR is quite strong in this quasar.

4 THE QUASAR NARROW-LINE REGION

We call here the NLR, the region of the quasar host galaxy that is located within the Point Spread Function (PSF) of the observations. This corresponds to about 1 arcsec or 7.1 kpc at the redshift of the quasar (or a distance of 3.55 kpc on both sides of the quasar). The emission seen beyond this will be called extended emission. We have shown that the DLA is of much smaller dimension so that most of the Lyman α NLR is not covered and is detected as Lyman α emission in the bottom of the DLA trough. We can extract this emission which is shown in the top panel of Fig. 8. It can be seen that the emission is spread over more than 1200 km s^{-1} with FWHM ~900 km s^{-1}.

4.1 C IV partial coverage

The large rest equivalent width of the C IV and Si IV absorption doublets and the flat-bottomed structure of their profiles suggest that these lines are saturated (see Fig. 8). However, the flux at the bottom of the C IV doublet absorption lines apparently does not reach the zero flux level, indicating that the absorbing cloud is only partially covering the background emission-line region.

When partial coverage occurs, the residual intensity seen at the bottom of absorption lines can be written as at each wavelength:

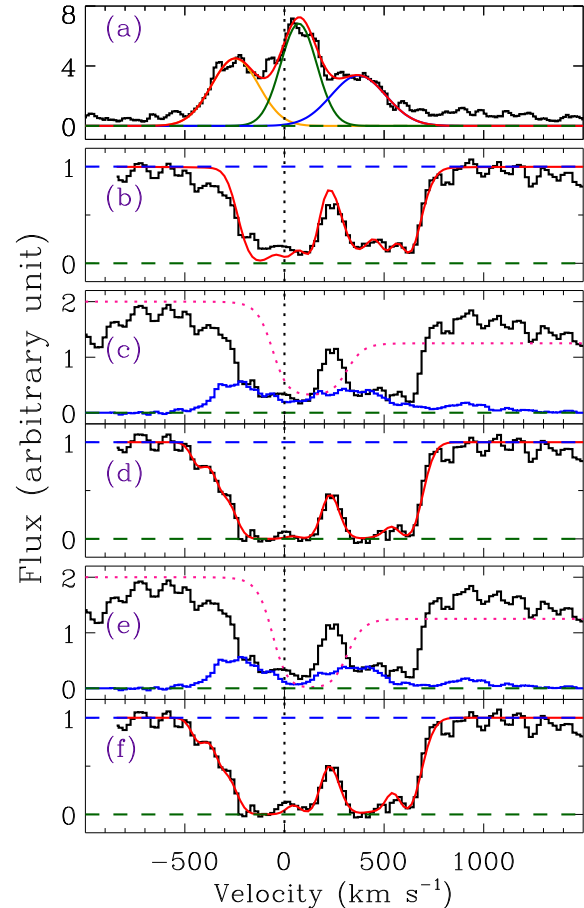$$I(\lambda) = I_0(\lambda)(1 - C_f) + C_f I_0(\lambda)\exp[-\tau(\lambda)], \quad (2)$$

Figure 8. Panel (a): Lyman α emission-line profile detected in the trough of the DLA. Three Gaussian functions are used to fit the profile. Panel (b): C IV absorption profiles (the two absorption lines C IV λ1548 and C IV λ1550 are seen). It is apparent from the flat bottom of the lines and similar apparent optical depths that the covering factor of the C IV gas is not unity. This is demonstrated by the model fit overplotted as a red line. Note that a Fe II λ2586 component at $z_{\rm abs} = 1.5140$ is blended in the red wing of the C IV λ1550 profile. Panel (c): the residual at the bottom of the C IV lines is fitted by scaling the Lyman α emission profile. The red dotted line indicates (on an arbitrary scale) the scaling factor (see equation (4)). The effective values of the C IV/Lyman α ratio are fitted to be 0.29, 0.045, and 0.18 for the three emission components, respectively. The C IV/Lyman α ratio must be much smaller in the second emission component. Panel (d): fit of the C IV doublet once the residuals (including both C IV emission lines) are removed. Panel (e): same as panel (c) but the central Lyman α component is supposed to have no C IV associated. Panel (f): fit of the C IV doublet once the residuals from panel (e) are removed (no C IV is associated with the central Lyman α component).

where $I_0(\lambda)$ is the incident (unabsorbed) intensity, $\tau(\lambda)$ is the optical depth of the cloud at the considered wavelength, and C_f is the fraction of the background emitting region that is covered by the absorbing cloud (i.e. the covering factor). In the case of doublets, and assuming the covering factor is the same for each component of the doublet, we can write:

$$C_f = \frac{1 + R_2^2 - 2R_2}{1 + R_1 - 2R_2}, \quad (3)$$

where R_1 and R_2 are the normalized residual intensities in the two absorption lines of the doublet (Petitjean & Srianand 1999; Srianand & Shankaranarayanan 1999).
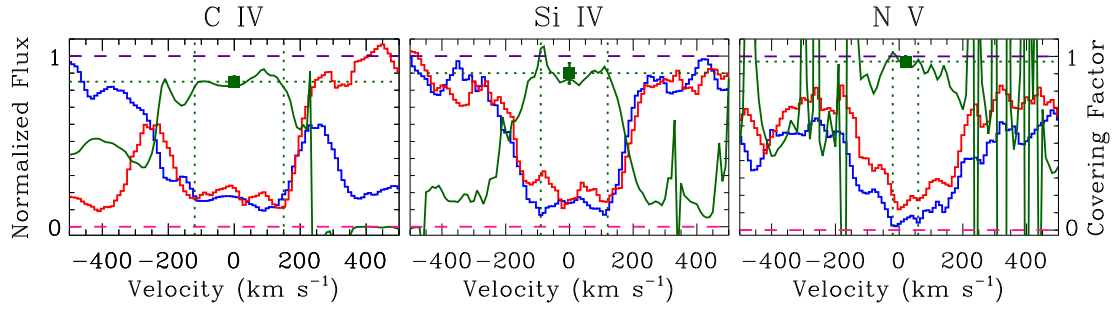
Figure 9. Covering factor estimations for C IV, Si IV, and N V doublets following equation (3). Vertical dashed lines indicate the windows in which it is calculated and horizontal dashed lines (and filled squares) give the mean over these windows. The red and blue histograms are the profiles of the weaker and stronger transitions of each doublet, respectively.

In Fig. 9, we show the covering factor of the C IV, Si IV, and N V doublets. Here, the red and blue histograms are the profiles of the weaker and stronger transitions of each doublet, respectively. The green solid line is the covering factor at each point of the profile calculated from equation (3). The green vertical dotted lines mark the regions used to calculate the mean values of C_f, avoiding the wings of the profiles. The green horizontal dotted lines along with the green filled squares show these mean values. Error bars are calculated as the standard deviation of C_f in different velocity bins. The measured values of C_f for C IV and Si IV are ∼0.85 and 0.90, respectively, suggesting that the size of the corresponding BEL region may be similar for the two high-ionization species. Note also that N V on the contrary seems fully covered.

The above numbers are however only indicative because the resolution of our spectrum is not high ($R \sim 4000$). In addition there is a possible Fe II λ2586 line at $z_{abs} = 1.5140$ blended with the red wing of C IV λ1550 (cyan curve in the C IV λ1550 panel in Fig. 2). In Fig. 8, we demonstrate the effect of partial coverage on the observed C IV doublet profiles taking into account the resolution of the spectrum and the presence of the Fe II line. The contribution of the Fe II λ2586 absorption to this fit is robustly determined by fitting together Fe II λλ2344, 2600 in the same system. In panel (b) of Fig. 8, the red curve is the fit conducted with VPFIT[3] on the original data. Here, we can see that there is no way to fit most of the profile without invoking partial coverage.

4.2 Reconstructing C IV narrow-emission-line (NEL) profile

As mentioned earlier, the flux at the bottom of the C IV doublet absorption lines does not reach the zero level. This residual flux could be due to the partial coverage of either the C IV BLR or NLR. However, the radius of the C IV phase associated with the DLA is larger and sometimes much larger than the size of the BLR (see Section 3.2) which strongly suggests that the residual flux is due to the C IV NLR.

We thus tried to reproduce the residual by C IV emission, including *both* lines of the doublet. Doing this we would like to ask the question whether we can associate the emission with the Lyman α emission. Indeed, this could bring important clues on the origin of the Lyman α emission. In case the Lyman α emission *cannot* be associated with C IV emission then this would strongly suggest that the Lyman α emission corresponds to scattered light after radiative transfer.

We thus first try to simply scale the Lyman α profile. This is bound to fail as it is apparent that the residuals do not follow the shape of the Lyman α emission. We therefore decomposed the Lyman α profile in three Gaussian functions (see top panel of Fig. 8) as suggested by the profile itself.

This allows us to scale different parts of the Lyman α profile differently. For each pixel, we define the ratio $R = $ C IV/Lyman α by combining the three Gaussian functions using the following equation:

$$R = \frac{R_1 \times G_1 + R_2 \times G_2 + R_3 \times G_3}{G_1 + G_2 + G_3}, \qquad (4)$$

where R_1, R_2, and R_3 are the weights for each component directly related to the C IV/Lyman α ratio in this component. By assigning different values to R_1, R_2, and R_3, we can scale each Gaussian individually. For instance, if $R_1 = R_2 = R_3 = 1.0$, this results in the red profile shown in panel (a) of Fig. 8. which is simply the combination of the three Gaussian functions. One can now use the factor $R = $ C IV/Lyman α defined for each wavelength to properly scale the Lyman α NEL profile. We thus have to adjust the R_1, R_2, and R_3 parameters until the C IV emission is consistent with the residual seen at the bottom of the C IV doublet absorption lines.

We find that the residual can be reproduced (see panel c of Fig. 8) with $R_1 = 0.29$, $R_2 = 0.045$, and $R_3 = 0.18$. The variation of R through the profile is given as a dashed pink line in panels (c) and (e) of Fig. 8. The corresponding fit of C IV after removing the residuals is given in panels (d) and (f).

Since the weight of the second emission component is much smaller than the two other ones, we ask the question whether it would be possible that the second component has no C IV associated. To test this, we impose $R_2 = 0.001$. The result of the fit is given in panels (e) and (f). It is apparent that we can find a solution with no C IV associated with the second component.

We thus conclude from all this that (i) the C IV emission is strongest around $v \sim -200\,\mathrm{km\,s^{-1}}$; this position could indicate the redshift of the quasar, implying that most of the Lyman α emission and the DLA are redshifted; (ii) at least part of the NLR Lyman α emission has no C IV emission associated (predominantly around $v = +100\,\mathrm{km\,s^{-1}}$) which means that the Lyman α emission in this component is due to scattered light or that the emitted gas is located within a distance from the quasar smaller than the transverse size of the C IV phase associated with the cloud so that the corresponding C IV emission is absorbed by the high-ionization phase of the DLA cloud.
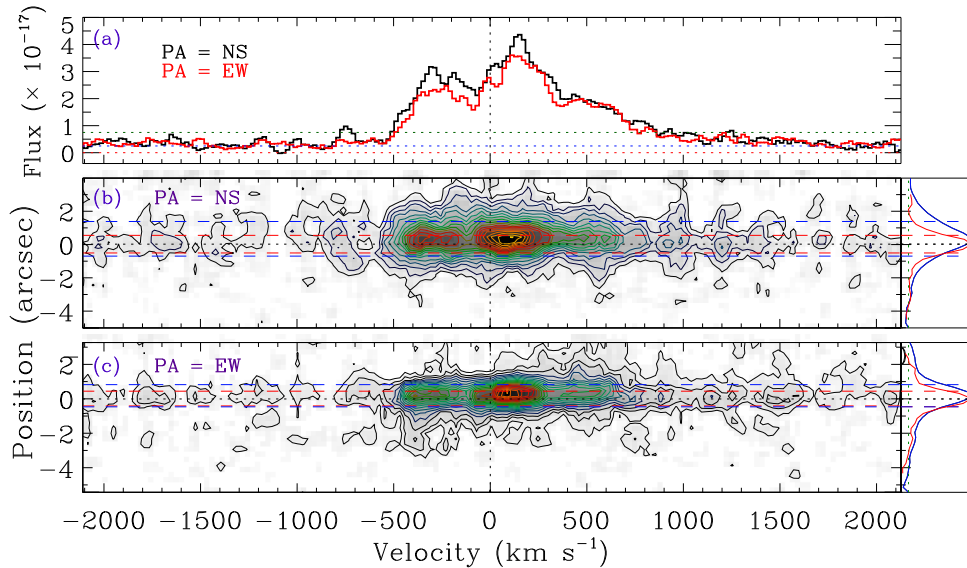
Figure 10. Panel (a): 1D spectrum showing the Lyman α emission in the bottom of the DLA trough. Black and red histograms are for PA = NS and EW, respectively. Red, blue, and green horizontal dotted lines mark the zero flux level, 1σ, and 3σ uncertainty on the flux, respectively. Panels (b) and (c): 2D spectra of the Lyman α emission seen in the trough of the DLA at $z_{abs} = 3.1910$ for PA = NS (panel b) and PA = EW (panel c). The contours show the observed flux density with a separation between two lines of 3.5×10^{-19} erg s^{-1} cm^{-2} Å^{-1}. The outermost contour corresponds to a flux density of 4.37×10^{-19} erg s^{-1} cm^{-2} Å^{-1}. The black horizontal dotted line shows the centre of the continuum trace. The blue and red dashed horizontal lines show the FWHM of the trace and extended Lyman α emission, respectively. Panels on the right show the spatial emission profile integrated over the whole wavelength range (blue curves) together with the continuum PSF (red lines) derived from the red part of the order. Note that in panel (a), the y-axis is in erg s^{-1} cm^{-2} Å^{-1}.

5 EXTENDED LYMAN α EMISSION

In the middle and bottom panels of Fig. 10, we show the 2D spectra of the Lyman α emission detected in the DLA trough for the two PAs. It is apparent that the Lyman α emission is extended and slightly displaced relative to the quasar trace. To quantify this, we integrate the whole Lyman α profile in the spectral direction and compare the result to the spatial PSF derived from the integration of the quasar spectrum over the rest of the order beyond 6520 Å. This is shown in the right-hand panels in Fig. 10. It is apparent that the emission is extended well beyond the PSF for both PAs and mostly in one direction implying that the total emission is shifted towards this direction.

We investigate whether the extension of the emission varies with the velocity position. For this, we split the velocity range over which the emission is seen in several regions, following the profile, and integrate the spatial emission profile over these regions. We then fit the profile by a Gaussian function. The results show that along PA = NS the spatial extent of the emission is larger than 5 arcsec over about 2000 km s^{-1} and that the shift is about 0.2 arcsec towards the north direction in the same region. For PA = EW, extension is about the same but the shift is consistent with zero meaning that the extended emission is more symmetric around the trace. The Lyman α emission is detected up to more than 25 kpc from the quasar and there is a strong excess emission along PA = NS to the north.

To better visualize the extended emission, we will subtract the emission associated with the central PSF, e.g. the emission located on the quasar trace. To do so, the 2D spectral order outside the Lyman α region of each PA is split into several chunks, and in each chunk the counts are integrated along the spectral axis. A Gaussian is then fitted on the profiles to get the central pixel values of the spatial profiles. Finally, we fit a straight line on these values to determine the centre of the trace for each spectral pixel.

Once we know the position of the trace exactly, we extract the spatial profile in each wavelength pixel and we fit a Gaussian with width equal to the continuum PSF width. We then subtract this Gaussian from the profile. Results are given in Fig. 11. Top panels show the resulting 2D spectrum of the extension. Bottom panels show the Lyman α profiles integrated along the spectral direction: in red the emission which was fitted on top of the trace and in black is the extension.

Along PA = NS, most of the extended emission is seen to the north up to projected distances of 3.5 arcsec or $\sim$25 kpc from the centre. The striking observation here is that the emission is extended over more than 1000 km s^{-1} at all distances from the quasar. Along PA = EW, extension is more apparent in one direction as well, to the west. However the velocity extension gets smaller when the distance to the quasar increases. Fig. 12 shows the variation of the integrated flux with distance. In this figure, the red and blue curves indicate variations of flux with distance following the relation $F = F_0(r/r_0)^{-2}$ relation. The data roughly follow such a law. In case this emission is due to recombination and since the ionization flux is decreasing with distance as r^{-2} this would mean that the number of ionized hydrogen atoms intersected by the slit is the same at all distances. This could be the case if the gas is clumpy so that changes in density has little effect.

The velocity profiles of the extended Lyman α emission at different distances from the AGN are shown in Fig. 13 and Table 4 summarizes the integrated flux and luminosity of the trace and the extension.

6 DISCUSSION AND CONCLUSIONS

We have performed slit spectroscopic observations of QSO J0823+0529 with the MagE spectrograph mounted on the Magellan telescope along two PAs, in the north–south and east–west
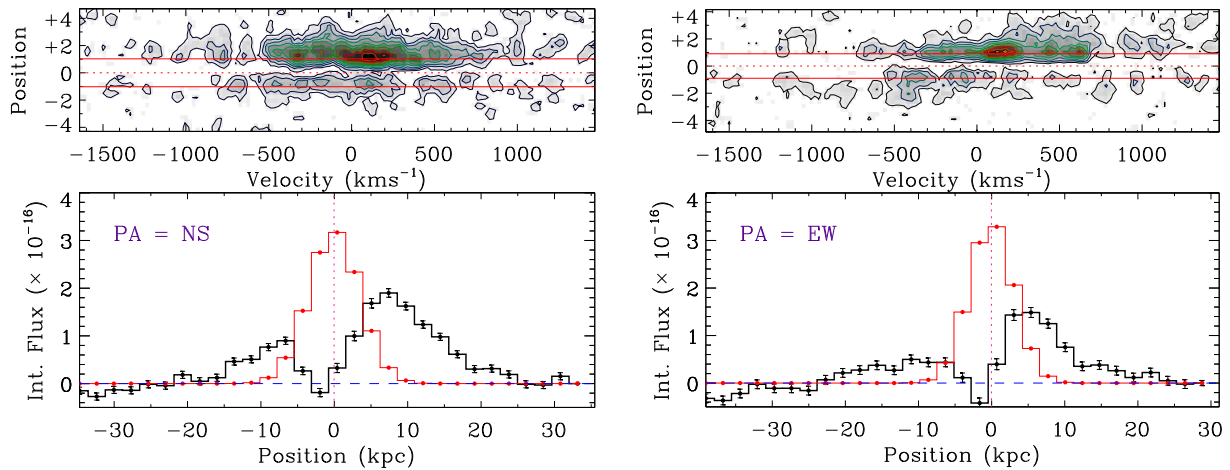
Figure 11. Upper panels: 2D spectra of the Lyman α emission seen in the trough of the DLA (left PA = NS and right PA = EW) after subtracting the emission in the PSF centred on the quasar trace. The contour levels are the same as in Fig. 10. The red horizontal dotted line shows the centre of the trace and the red solid horizontal lines show the FWHM of the trace. Bottom panels: emission profiles integrated over the whole wavelength window of the Lyman α emission in the PSF centred on the quasar trace (red histograms) and the extended emission (black histograms). Note that in the upper (resp. lower) panels, the *y*-axis is in arcsec (resp. erg s^{-1} cm^{-1} arcsec^{-2}).
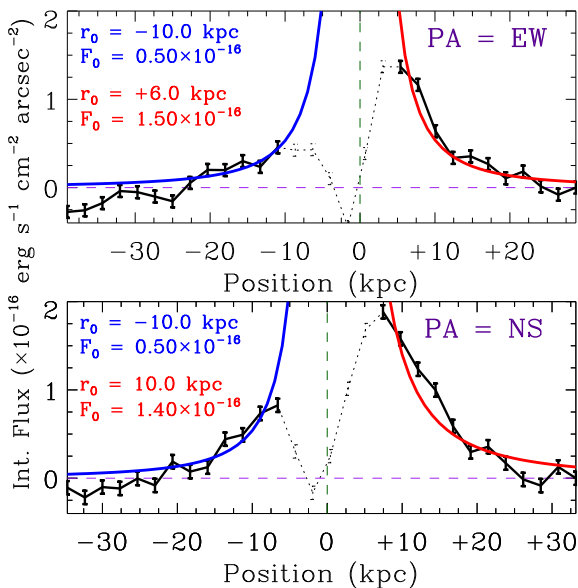

Figure 12. Variations of the integrated Lyman α flux with distance from the AGN. The black lines with error bars are the observations and the red and blue curves indicate a variation of the flux with distance following a r^{-2} relation. Note that in both panels F_0 is in erg s^{-1} cm^{-2} arcsec^{-2}.

directions. The quasar is unique because a DLA is located at a redshift very similar to that of the quasar ($z_{DLA} = 3.1910$ and $z_{CIV} = 3.1875$, i.e. $\Delta v \sim 330$ km s^{-1}) and acts as a coronagraph blocking most of the flux from the central regions of the AGN. In the present case, the DLA cloud is small enough so that it covers only approximately 90 per cent of the Lyman α BLR. This puts us in a unique position to be able to directly observe the quasar NLR and the extended emission-line region. Indeed, Lyman α emission is detected up to more than 25 kpc from the quasar along both PAs.

6.1 The quasar NLR

Finley et al. (2013) have gathered a sample of 57 DLAs acting as a coronagraph in front of quasars; the DLAs have redshifts within

1500 km s^{-1} from the quasar redshift. Their statistical sample of 31 quasars shows an excess of such DLAs compared to what is expected from the distribution of intervening DLAs. This can be explained if most of these DLAs are part of galaxies clustering around the quasar. However, 25 per cent of such DLAs reveal Lyman α emission probably from the quasar host galaxy implying that these DLAs have sizes smaller than the quasar emission region. The Lyman α luminosities are consistent with those of Lyman α emitters in 75 per cent of the cases and 25 per cent have much higher luminosities. The later systems probably reveal the central NLR of the quasar. QSO J0823+0529 is part of this later class of coronagraph DLAs.

We have shown that the size of the neutral phase is of the order of 2–9 pc which means that the gas does not cover the Lyman α NLR. Three main components of Lyman α emission from the NLR are clearly detected at $\Delta V = -300$, $+100$, and $+400$ km s^{-1} relative to the DLA redshift (see Fig. 9). The corresponding C IV emission seems to be absent in the second strongest component. Either the Lyman α emission is scattered or the associated C IV emission is absorbed by the high-ionization phase of the DLA. To be covered, the corresponding gas must be located within ∼3–80 pc from the quasar which, we have seen, corresponds to the extension of the high-ionization phase of the cloud assuming spherical geometry. At least part of the two other components could therefore be located beyond this distance from the quasar, although part of the third component could also be hidden, as the C IV/H I ratio is larger by a factor of about 2 in the first component compared to the third component (see Fig. 9). Note that the relative velocities of components 1 and 3 can be interpreted as the result of a conical outflow with mean projected velocities of about ±300 km s^{-1}.

6.2 Lyman α emission from the centre to the outskirts of the host galaxy

Extended Lyman α emission has been observed around high-redshift radio galaxies (Heckman et al. 1991; van Ojik et al. 1996), as well as around radio-quiet quasars (Bunker et al. 2003; Christensen et al. 2006). For radio-loud quasars or radio galaxies, the Lyman α flux of the nebula is an order of magnitude higher
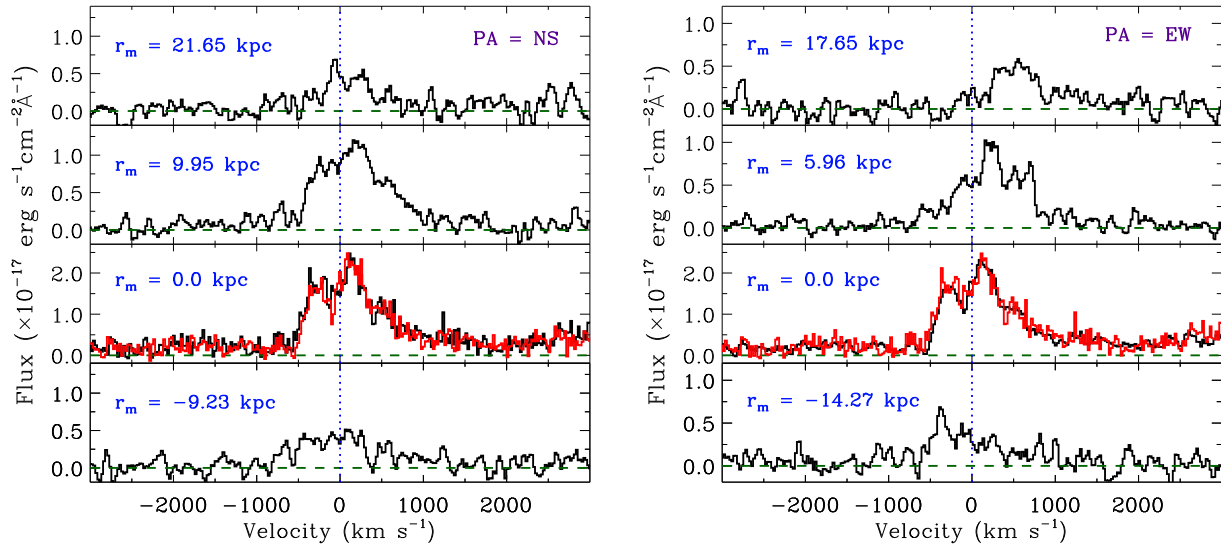
Figure 13. Velocity profiles of the extended Lyman α emission at different distances from the AGN for PA = NS (left-hand panels) and PA = EW (right-hand panels). The parameter r_m gives the mean distance to the AGN. The red histogram in the left-hand panel (resp. right-hand panel) shows the spectrum of the trace for the PA = EW (resp. PA = NS).

Table 4. Lyman α integrated fluxes and luminosities in the PSF centred on the quasar trace and in the extension. The last row gives the integrated flux and luminosity of the broad Lyman α emission calculated using the simulated spectrum shown in Fig. 7.

	Integrated flux [erg s^{-1} cm^{-2}]	Luminosity [erg s^{-1}]
Trace(PA = NS)	3.59×10^{-16}	3.43×10^{43}
Extension(PA = NS)	3.97×10^{-16}	3.79×10^{43}
Trace(PA = EW)	3.36×10^{-16}	3.21×10^{43}
Extension(PA = EW)	2.68×10^{-16}	2.56×10^{43}
Lyman α(BELR)	7.10×10^{-15}	6.78×10^{44}

(Christensen et al. 2006), presumably because the emission of radio-loud quasar gaseous envelopes is enhanced by interactions with the radio jets. More recently, North et al. (2012) have used a careful treatment of the spectral PSF to extract quasar traces. This revealed four detections of extended emission out of six radio-quiet quasars at $z \sim 4.5$ with extensions of diameter $16 < d < 64$ kpc down to a luminosity of 2×10^{-17} erg s^{-1} cm^{-2} arcsec^{-2}. The emission has $900 < $ FWHM < 2200 km s^{-1}. Our observations are in line with these numbers. The extended emission we detect in QSO J0823+0529 has a diameter of ~ 50 kpc and FWHM ~ 900 km s^{-1}. However, QSO J0823+0529 does not seem to follow the L(Lyman α) versus L(BLR) relation indicated by these authors. Indeed the Lyman α luminosity in QSO J0823+0529 is more than an order of magnitude larger than what would be expected from this relation even after correcting for dust attenuation. It is still possible that dust is present closer to the quasar and further attenuates the BLR Lyman α emission. It is also possible that the decomposition between the BLR and NLR emissions was ambiguous in previous studies so that the NLR emission could have been underestimated.

The emission is more extended to the north–west of the object (see Figs 11 and 13). There are two notable features in the spatial and velocity structure of the nebula. First, in the north–west direction, the kinematics are strikingly similar along the trace and 10 kpc away from the centre (see Fig. 13) with a velocity spread of more than 1000 km s^{-1}. The emission is quite strong in this region. Secondly,

there is a clear gradient of about 1000 km s^{-1} between 15 to the east and 20 kpc to the west. It is tempting to interpret these features as the superposition of the emission of gas in the disc of the galaxy, where the density is higher and turbulent kinematics prevent gas clouds to be well organized with emission from gas flowing out of the disc with velocities of the order of 500 km s^{-1}. This gas is best seen up to 20 kpc to the west and 10 kpc to the east. Such winds can be reproduced by recent models taking into account the effects of radiation trapping (Ishibashi & Fabian 2015).

6.3 Nature of the DLA

It is well demonstrated that bright quasars are surrounded by large amounts of gas both in extended ionized haloes up to 10 Mpc from the quasar (e.g. Rollinde et al. 2005) and extended (300 kpc) reservoirs of neutral gas in the halo of the host galaxy (Prochaska, Hennawi & Simcoe 2013; Prochaska, Lau & Hennawi 2014; Johnson, Hsiao-Wen & Mulchaey 2015). However, along the line of sight to quasars, the incidence of neutral gas is less (e.g. Shen & Ménard 2012) indicating that the ionizing emission from quasars is highly anisotropic. The DLA we discuss here is part of the so-called proximate DLAs in the sense that the absorption redshift is similar to that of the quasar ($z_{abs} \sim z_{em}$, see e.g. Ellison et al. 2010). However, this is the first time it can be demonstrated that the gas is located very close to the quasar (<400 pc) and probably associated with the central part of the host galaxy.

We have modelled the physical state of the gas in the DLA using photoionization models. The ionization parameter is found to be in the range $-1.1 < \log U < +0.3$ which means that the cloud is mostly highly ionized. A density of $n_H \sim 710$–180 cm^{-3} is needed to explain the absorption lines from O I and Si II ground state excited levels implying that the neutral phase should have dimensions of the order of 2–9 pc and be embedded in an ionized cloud of size ~ 3–80 pc. From this, we could derive that the cloud is located between 230 and 580 pc from the quasar. The metallicity of the cloud, $Z = 0.16$ Z$_\odot$, is typical of the metallicity of standard intervening DLAs (Rafelski et al. 2012).

It is intriguing to note that the high-ionization phase of the cloud we see has characteristics similar to those of some of the WAs seen in many AGNs. Tombesi et al. (2013) argued that WAs and ultra-fast outflows (UFO) could represent parts of a single large-scale stratified outflow observed at different locations from the black hole. The UFOs are likely launched from the inner accretion disc and the WAs at larger distances, such as the outer disc and/or torus. There are still significant uncertainties on the exact location of this material, which ranges from a few pc up to kpc scales (e.g. Krolik & Kriss 2001; Blustin et al. 2005). The absorption lines are systematically blue-shifted, indicating outflow velocities of the WAs in the range 100–1000 km s^{-1}. King & Pounds (2014) have argued that the dense gas which surrounds the AGN when it starts shining is swept out by the fast winds powered by the accretion luminosity. The wind is halted by collisions near the radius where radiation pressure drops. The shocked gas must rapidly cool and mix with the swept-up ISM. Distance from the AGN and properties of the gas are similar to what is observed for WAs, as in our case. Therefore, in QSO J0823+0529, the DLA could be located in the galactic disc at the terminal position of the wind, at the limit of the ISM of the host galaxy. The presence of dust in the gas can be considered as supporting this view as it is expected in the dense environment of AGNs (see e.g. Leighly et al. 2015).

The only caveat with this idea is that the metallicity of the DLA is typical of intervening DLAs, when we would expect the gas in the ISM of the quasar host galaxy to have larger metallicity. This, together with the low outflow velocity (the DLA is centred on the Lyman α emission), argues for another explanation for the origin of this gas. Given the distance to the central AGN ($230 < r_0 < 580$ pc), one is tempted to conjecture that it could be the final fate of infalling gas. Note that in that case, the presence of dust is not a problem as the observed amount is not unusual compared to what is seen in typical high column density DLAs. Indeed, accretion is believed to happen through cold flows which are expected to be of lower metallicity compared to the environment of the quasar (see Bouché et al. 2013). Little is known about how quasars at high redshift interact with cold infalling streams of gas, and in particular whether these collimated structures can survive the energy released by the AGN. Therefore the DLA cloud could be in a transitory phase before it is completely destroyed by the AGN ionizing radiation field (Namekata, Umemura & Hasegawa 2014).

The two alternatives are actually not incompatible, since some of the WAs could be part of the galactic ISM swept away from the centre by the AGN and placed at large distances from the AGN (e.g. King & Pounds 2014). These outflowing WAs may then intersect with accreted cold streams.

6.4 Concluding remark

There is little doubt that DLAs acting as coronagraphs are important targets to be observed and analysed. Besides revealing interesting characteristics of the quasar host galaxy they are, like in QSO J0823+0529, potentially part of the machinery that power the AGN. Finley et al. (2013) found 57 such systems out of about a third of the BOSS targets. With the ongoing eBOSS-SDSSIV survey and the foreseen DESI survey (Schlegel, Abdalla & Abraham 2011), the number of such systems will increase by a large factor in the future. It will thus be important to gather a large sample of these objects to be able to study their characteristics statistically.

REFERENCES

Asplund M., Grevesse N., Sauval A. J., Scott P., 2009, ARA&A, 47, 481
Bentz M. C., Peterson B. M., Netzer H., Pogge R. W., Vestergaard M., 2009a, ApJ, 697, 160
Bentz M. C., Walsh J. L., Barth A. J., Baliber N., Bennert V. N. et al., 2009b, ApJ, 705, 199
Blustin A. J., Page M. J., Fuerst S. V., Branduardi-Raymont G., Ashton C. E., 2005, A&A, 431, 111
Bouché N., Murphy M. T., Kacprzak G. G., Péroux C., Contini T., Martin C. L., Dessauges-Zavadsky M., 2013, Science, 341, 50
Bunker A., Smith J., Spinrad H., Stern D., Warren S., 2003, Ap&SS, 284, 357
Chartas G., Saez C., Brandt W. N., Giustini M., Garmire G. P., 2009, ApJ, 706, 644
Chen H.-W., Prochaska J. X., Bloom J. S., Thompson I. B., 2005, ApJ, 634, L25
Christensen L., Jahnke K., Wisotzki L., Sánchez S. F., 2006, A&A, 459, 717
Crenshaw D. M., Kraemer S. B., George I. M., 2003, ARA&A, 41, 117
Dai X., Kochanek C. S., Chartas G., Kozowski S., Morgan C. W., Garmire G., Agol E., 2010, ApJ, 709, 278
Dawson K. S. et al., 2013, AJ, 145, 10
Dubois Y., Pichon C., Devriendt J., Silk J., Haehnelt M., Kimm Taysun, Slyz A., 2013, MNRAS, 428, 2885
Ellison Sara L., Prochaska J. X., Hennawi J., Lopez S., Usher C., Wolfe A. M., Russell D. M., Benn C. R., 2010, MNRAS, 406, 1435
Fathivavsari H., Petitjean P., Ledoux C., Noterdaeme P., Srianand R., Rahmani H., Ajabshirizadeh A., 2013, MNRAS, 435, 1727
Faucher-Giguère C.-A., Quataert E., 2012, MNRAS, 425, 605
Finley H. et al., 2013, A&A, 558, 111
Fynbo J. P. U. et al., 2006, A&A, 451, L47
Gofford J., Reeves J. N., Tombesi F., Braito V., Turner T. J., Miller L., Cappi M., 2013, MNRAS, 430, 60
Haardt F., Madau P., 1996, ApJ, 461, 20
Hainline L. J. et al., 2013, ApJ, 774, 69
Harrison C. M., Alexander D. M., Mullaney J. R., Swinbank A. M., 2014, MNRAS, 441, 3306
Heckman T. M., Lehnert M. D., Miley G. K., van Breugel W., 1991, ApJ, 381, 373
Hennawi J. F., Prochaska J. X., Kollmeier J., Zheng Z., 2009, ApJ, 693, L49
Hewett P. C., Wild V., 2010, MNRAS, 405, 2302
Hu E. M., Cowie L. L., 1987, ApJ, 317, L7
Hu E. M., McMahon R. G., Egami C., 1996, ApJ, 459, L53
Ishibashi W., Fabian A. C., 2015, MNRAS, 451, 93
Johnson S. D., Chen H.-W., Mulchaey J. S., 2015, MNRAS, 452, 2553
Kaspi S., Maoz D., Netzer H., Peterson B. M., Vestergaard M., Jannuzi B. T., 2005, ApJ, 629, 61
Kelson D. D., 2003, PASP, 115, 688
King A., Pounds K., 2014, MNRAS, 437, 81
King A., Pounds K., 2015, preprint (arXiv:1503.05206)
Komatsu E. et al., 2011, ApJS, 192, 18
Kornei K. A., Shapley A. E., Erb D. K., Steidel C. C., Reddy N. A., Pettini M., Bogosavljević M., 2010, ApJ, 711, 693
Krolik J. H., Kriss G. A., 2001, ApJ, 561, 684
Leighly K. M., Cooper E., Grupe D., Terndrup D. M., Komossa S., 2015, ApJ, 809, 13

Marshall J. L. et al., 2008, in McLean I. S., Casali M. M., eds, Proc. SPIE Vol. 7014, Ground-based and Airborne Instrumentation for Astronomy II. SPIE, Bellingham, p. 701454

Mathews W. G., Ferland G. J., 1987, ApJ, 323, 456

Mullaney J. R., Alexander D. M., Fine S., Goulding A. D., Harrison C. M., Hickox R. C., 2013, MNRAS, 433, 622

Namekata D., Umemura M., Hasegawa K., 2014, MNRAS, 443, 2018

Neeleman M., Prochaska J. X., Wolfe A. M., 2015, ApJ, 800, 7

North P. L., Courbin F., Eigenbrod A., Chelouche D., 2012, A&A, 542, 91

Noterdaeme P., Srianand R., Rahmani H., Petitjean P., Pâris I., Ledoux C., Gupta N., López S., 2015, A&A, 577, 24

Pâris I. et al., 2011, A&A, 530, 50

Pâris I. et al., 2012, A&A, 548, 66

Pâris I. et al., 2014, A&A, 563, 54

Petitjean P., Pécontal E., Valls-Gabaud D., Charlot S., 1996, Nature, 380, 411

Petitjean P., Srianand S., 1999, A&A, 345, 73

Prochaska J. X., Hennawi J. F., Simcoe R. A., 2013, ApJ, 762, L19

Prochaska J. X., Lau M. W., Hennawi J. F., 2014, ApJ, 796, 140

Rafelski M., Wolfe A. M., Prochaska J. X., Neeleman M., Mendez A. J., 2012, ApJ, 755, 89

Rauch M., Becker G. D., Haehnelt M. G., Carswell R. F., Gauthier J.-R., 2013, MNRAS, 431, 68

Rollinde E., Srianand R., Theuns T., Petitjean P., Chand H., 2005, MNRAS, 361, 1015

Schlegel D., Abdalla F., Abraham T., 2011, preprint (arXiv1106.1706)

Shen Y., Ménard B., 2012, ApJ, 748, 131

Srianand R., Shankaranarayanan S., 1999, ApJ, 518, 672

Srianand R., Petitjean P., 2000, A&A, 357, 414

Tombesi F., Cappi M., Reeves J. N., Nemmen R. S., Braito V., Gaspari M., Reynolds C. S., 2013, MNRAS, 430, 1102

van Ojik R., Roettgering H. J. A., Carilli C. L., Miley G. K., Bremer M. N., Macchetto F., 1996, A&A, 313, 25

Vreeswijk P. M. et al., 2004, A&A, 419, 927

Weidinger M., Moller P., Fynbo J. P. U., Thomsen B., 2005, A&A, 436, 825

Wu X.-B., Wang R., Kong M. Z., Liu F. K., Han J. L., 2004, A&A, 424, 793

This paper has been typeset from a TEX/LATEX file prepared by the author.